Journal of Applied Physics

Interfacial sharpness and intermixing in a Ge-SiGe multiple quantum well structure

Cite as: J. Appl. Phys. **123**, 035703 (2018); https://doi.org/10.1063/1.5001158
Submitted: 22 August 2017 . Accepted: 27 December 2017 . Published Online: 19 January 2018

A. Bashir, K. Gallacher, R. W. Millar, D. J. Paul, A. Ballabio, J. Frigerio, G. Isella, D. Kriegner, M. Ortolani, J. Barthel, and I. MacLaren

Interfacial sharpness and intermixing in a Ge-SiGe multiple quantum well structure

A. Bashir,[1] K. Gallacher,[2] R. W. Millar,[2] D. J. Paul,[2] A. Ballabio,[3] J. Frigerio,[3] G. Isella,[3] D. Kriegner,[4,5] M. Ortolani,[6] J. Barthel,[7] and I. MacLaren[1]
[1]*School of Physics and Astronomy, University of Glasgow, Kelvin Building, University Avenue, Glasgow G12 8QQ, United Kingdom*
[2]*School of Engineering, University of Glasgow, Rankine Building, Oakfield Avenue, Glasgow G12 8LT, United Kingdom*
[3]*L-NESS, Dipartimento di Fisica del Politecnico di Milano, Polo Territoriale di Como, Via Anzani 42, Como I-22100, Italy*
[4]*Institute of Physics ASCR, v.v.i., Cukrovarnická 10, 162 53 Praha 6, Czech Republic*
[5]*Faculty of Mathematics and Physics, Charles University, Ke Karlovu 3, 121 16 Prague 2, Czech Republic*
[6]*Center for Life NanoScience@Sapienza, Istituto Italiano di Tecnologia, Viale Regina Elena 291, Rome I-00161, Italy*
[7]*Ernst Ruska-Centre (ER-C) for Microscopy and Spectroscopy with Electrons, Forschungszentrum Jülich GmbH, 52425 Jülich, Germany*

(Received 22 August 2017; accepted 27 December 2017; published online 19 January 2018)

A Ge-SiGe multiple quantum well structure created by low energy plasma enhanced chemical vapour deposition, with nominal well thickness of 5.4 nm separated by 3.6 nm SiGe spacers, is analysed quantitatively using scanning transmission electron microscopy. Both high angle annular dark field imaging and electron energy loss spectroscopy show that the interfaces are not completely sharp, suggesting that there is some intermixing of Si and Ge at each interface. Two methods are compared for the quantification of the spectroscopy datasets: a self-consistent approach that calculates binary substitutional trends without requiring experimental or computational *k*-factors from elsewhere and a standards-based cross sectional calculation. Whilst the cross section approach is shown to be ultimately more reliable, the self-consistent approach provides surprisingly good results. It is found that the Ge quantum wells are actually about 95% Ge and that the spacers, whilst apparently peaking at about 35% Si, contain significant interdiffused Ge at each side. This result is shown to be not just an artefact of electron beam spreading in the sample, but mostly arising from a real chemical interdiffusion resulting from the growth. Similar results are found by use of X-ray diffraction from a similar area of the sample. Putting the results together suggests a real interdiffusion with a standard deviation of about 0.87 nm, or put another way—a true width defined from 10%–90% of the compositional gradient of about 2.9 nm. This suggests an intrinsic limit on how sharp such interfaces can be grown by this method and, whilst 95% Ge quantum wells (QWs) still behave well enough to have good properties, any attempt to grow thinner QWs would require modifications to the growth procedure to reduce this interdiffusion, in order to maintain a composition of ≥95% Ge. *Published by AIP Publishing.*
https://doi.org/10.1063/1.5001158

I. INTRODUCTION

Integrating optics with electronics on-chip is a promising route for optoelectronics whilst overcoming the issues associated with electrical interconnects.[1,2] A significant challenge for high volume, large scale Electronic Photonic integrated circuits on Si (EPICs) is active photonic devices for light, modulation, and detection.[3] Despite extensive research on photonic devices based on Si, the difficulties associated with this technology, including narrow operational bandwidth, thermal instability,[4,5] and electrical injection limits, as well as low efficiency,[6,7] have demanded new development in the field. It is only recently that Ge has gathered much attraction from scientists for promising electronic and photonic applications due to its large compatibility with Si technology and its pseudodirect bandgap.[8–11] Energy band engineering through tensile strain[9–11] and utilization of direct gap transitions,[3] in Ge, have been successfully demonstrated in optical modulators [8,10,12] and lasers[11,13] in recent years. Moreover, rather than directly engineering the Ge material itself, Ge based multiple quantum well (MQW) device structures[13] and nanostructures[14] have also been explored to exploit their quantum confined properties. It is now established that Quantum Confined Stark effect (QCSE) based modulators using Ge/SiGe multiple quantum wells (MQWs) can fulfil all the requirements for monolithically integrated Si photonics modulators.[8,15,16] Ge/SiGe MQWs have also shown electro-absorption modulation over the telecommunication bands, and with less than 1 V total drive voltage, which is particularly important for minimizing energy dissipation.[17] Phase modulation has also been demonstrated in single QWs[18] and in coupled QWs heterostructures.[19] QCSE modulators integrated with Ge waveguides and photodetectors have also recently been realised.[20] Other than

modulation and detection, Ge/SiGe quantum well systems have demonstrated light emitting properties.[11,21,22] It is also interesting to note that a Ge QW system has shown promising qualities for cheap and practical sensors in the quantum well (QW) infrared photodetectors (QWIPs)[23,24] that cover the important transmission windows within the mid-infrared (MIR) (3–5 and 8–13 μm wavelength). Absorption occurring from intersubband transitions within the QW can be tuned by adjusting the QW width, thereby changing the energy of the confined subband states. This allows tuning strong absorption from the normally transparent semiconductors like Si and Ge in the MIR.[23–26]

Key parameters for such heterostructures are the Ge content and the quality of the interface for electronic/opto-electronic applications.[27] The quantum confinement effect is essentially associated with a sharp interface giving rise to an abrupt change in the potential for confined electrons and holes. A diffuse interface can bring about significant deviations from the ideal behaviour. Moreover this also results in I–V and optical characteristics resonance peak broadening.[28] Consequently, the device quality can be badly affected. That is why structural and chemical abruptness of the interfaces in quantum well heterostructures is of critical importance for device applications.[29,30]

One of the best methods of determining interface sharpness on individual interfaces with high spatial resolution is scanning transmission electron microscopy (STEM) combined with electron dispersive spectroscopy (EDS), electron energy loss spectroscopy (EELS), or quantitative high angle annular dark field (HAADF) intensity measurements.[31–35] Alternatively, one can use atom probe tomography (APT),[36,37] albeit with a much reduced field of view. These methods have been applied for composition analysis of various structures including nanowires and quantum wells based on Ge-Si and GaAs being the most studied systems. APT is a technique based on atom by atom field evaporation from a sharply pointed sample for analysis of morphology and composition in three dimensions. Nevertheless, different materials with different evaporation fields within 3D structures produce reconstruction artefacts, which can cause strong deviation from the original structure.[38] For example with interfaces, distorted reconstructed shapes are obtained and the measured local compositions may be incorrect due to ion trajectory overlaps.[39,40] STEM/EDS can be affected by an interaction volume much larger than the beam diameter as well as stray scattering from areas of the sample far from the probe. Quantitative HAADF-STEM uses quantification of high angle scattering intensities and comparison with simulations to interpret information about the composition. Materials with two or more alloying elements have been studied with high spatial resolution using this method.[32,33,41,42] Strain-induced contrast in HAADF, however, due surface relaxation and de-channelling[43] or due to diffuse scattering from defects[32] has often been ignored. This method is therefore indirect in that it depends on the correctness of element-substitution models and does critically rely on the image simulations correctly including the effects of strain.

In this paper, we have used STEM and EELS in order to perform compositional studies of pure Ge based MQWs. EELS has advantages over the other techniques for quantitative analysis, combining a similar spatial resolution to HAADF imaging with the direct quantification of element concentrations from the spectra, especially when performed on modern spectrometers on a STEM using fast spectrum imaging (SI).[44,45] Specific advantages are possible using the recently developed dual-range EELS (DualEELS) technique[46] available on recently introduced spectrometers in that absolute quantification is now possible due to having access to the low loss spectrum as well as to the core-loss edges. There are, however, a limited number of reports of the application of STEM EELS for compositional analysis of fine MQWs to date. Benedetti *et al.* analysed nominally $Si_{0.8}Ge_{0.2}$ quantum wells in Si using transmission electron microscopy (TEM) imaging, X-ray line traces, and EFTEM mapping and mainly focused on understanding why the SiGe-Si interface was broader than the Si-SiGe interface. Mkhoyan *et al.* used EELS to quantify that GaN/AlN QWs[31] and electron channelling simulations are combined with experiment to separate real interface widths from beam broadening. Ross *et al.*[47] studied $Si_{0.6}Ge_{0.4}$ QWs in Si using HAADF imaging and EELS line traces with an aberration-corrected STEM instrument and found that the two types of contrast followed quite well, and they also discovered that the interfaces were not completely sharp but the reasons for this were not examined in detail and the profiles were not modelled. Ge QWs embedded within rare earth oxide layers were analysed by Das and Bhattacharyya[29] although the interfaces in these QWs seem intrinsically sharper than those in SiGe-Si or mixed III–V structures, probably due to the chemical dissimilarity of the rare earth oxide and the Ge. In a very recent report, Longo *et al.*[48] combined EELS and cathodoluminescence to gain compositional as well as local luminescence information for GaN/InGaN QWs. There have been a larger number of studies of SiGe layers in Si,[49–52] but not necessarily as fine or as part of periodic MQW structures as in this work. Some of these studies found asymmetric elemental profiles on SiGe QWs with the SiGe-Si interfaces being broader than the Si-SiGe interfaces in chemical vapour deposition (CVD)-grown and MBE-grown layers; it seems free Ge atoms on the surface have a tendency to diffuse into the Si being laid down above in both processes. There may be additional issues with gas persistence in CVD during switching between Ge-rich and Si-rich layers.

The objective of this paper is to study the Ge distribution and composition variations in a Ge/SiGe MQWs structure in order to properly understand the compositional profiles. TEM specimen preparation has made it easy for quantitative STEM analysis of this structure. The work was performed on probe corrected STEM using EELS, and the quantitative analysis for MQWs was performed both using a standardless self-consistent approach as well as using experimentally determined cross sections from pure Si and Ge standards. The two approaches are compared and contrasted quantitatively, and it is demonstrated that the interfaces are not atomically sharp but show some roughness and interdiffusion over a few atomic planes, which is in agreement with analysis of X-ray diffraction data.

II. EXPERIMENTAL PROCEDURE

A. Quantum well growth

For this work, we have used a sample which was grown by low energy plasma enhanced chemical vapour deposition (LEPECVD) on a high resistivity Si (100) substrate and consisted of 500 periods of nominally 4.6 nm Ge quantum wells, QWs, separated by nominally 2.6 nm $Si_{0.5}Ge_{0.5}$ barrier layers (all doped to $N_A \approx 5 \times 10^{18}\,cm^3$). The bottom spacer region was a 500 nm thick $Si_{0.6}Ge_{0.4}$ layer followed by a 500 nm linear graded $Si_{1-x}Ge_x$ buffer from $x = 0.4$ until $x = 0.8$,[53] upon which the QW structure was grown at a deposition rate of 1 nm/s and a substrate temperature of 475 °C. The QW structure was capped by a 10 nm of undoped $Si_{0.2}Ge_{0.8}$ spacer layer, followed by another 20 nm of a $Si_{0.2}Ge_{0.8}$ cap layer. Further details can be found in the work of Gallacher *et al.*[25]

B. Microscopy specimen preparation

A cross section sample of controlled thickness was prepared for STEM using a focused ion beam (FIB, FEI Nova Nanolab 200) lift-out procedure.[54] After locating an area of interest, first it was coated with thin platinum (Pt) layer using the electron beam followed by a layer of Ga-beam deposited platinum to prevent milling or Ga-beam imaging from damaging the surface of the TEM specimen cross section. Then a 15 μm wide and 1 μm thick region of interest was undercut as a TEM lamella. All this was performed using a 30 kV Ga beam. This was carefully lifted out and attached to an Omniprobe support grid, prior to final milling and polishing. The TEM lamella was ion polished on both sides using a reduced beam current and progressively lower voltages down to 5 kV resulting in a final thickness at the edge of just a few nm. Moreover samples from pure Ge and pure Si were produced in a similar manner, but with final thinning angles adjusted to give deliberate wedge shaped cross sections for use as EELS standards.

C. Imaging and spectrum imaging

To study the heterostructure quality and composition of the QWs, STEM imaging and EELS were performed on a probe corrected JEOL ARM 200F equipped with a cold field emission gun operated at 200 kV and using a convergence half angle of 29 mrad. HAADF imaging was performed with an inner detector angle of 107 mrad. A Gatan GIF Quantum ER energy filter/spectrometer with fast DualEELS was used for recording of spectrum images (SIs) with a collection half angle of 36 mrad. All acquisitions were performed using the spectrum imaging plug-in for Gatan Digital Micrograph. The spot size was of the order of 2–3 Å with condenser settings chosen to give a probe current in the range 180 to 400 pA. A dispersion of 1 eV per channel was used.

D. X-ray diffraction experiments

To benchmark the STEM results, we performed high-resolution X-ray diffraction measurements using a PANalytical X'Pert PRO MRD equipped with a hybrid mirror and a 2-bounce asymmetric Ge monochromator selecting CuKα_1 radiation. Reciprocal space maps around the (004) and (224) Bragg diffraction peaks were recorded, as well as a symmetric radial scan through the (004) diffraction signals of the MQW, buffers, and substrate. A spot close to the location where the TEM lamellae were produced was chosen for the measurement.

III. ANALYTICAL METHODS

A. Layer thickness

The QW and barrier thicknesses were calculated using the HAADF signal variation across the structure. Unfortunately, sample or stage drift can affect the quality of scanned image data dramatically[55] as do environmental factors such as the temperature and pressure variations.[56] To overcome this and to increase the signal to noise ratio, a better approach for image acquisition is to record multiple frames rapidly over the same area and realign these using a cross correlation method.[55–59] In order to investigate quantitatively as to how uniform the thickness of the Ge QWs and the barrier layers are within the stack, 20 scans of the same area were obtained. First, a high quality sum image was calculated after cross correlating these scans using a specially designed software tool.[60] A profile of signal intensities, laterally averaged in the direction orthogonal to the growth direction, was then analysed to accurately evaluate the interlayer separation. The x intercepts to the median (50%) intensity values were extracted. The thickness profile of the active layers was then calculated as difference in x intercepts defining each QW and spacer layer in the intensity profile.

B. Compositional analysis

DualEELS data sets were used for qualitative and quantitative elemental mapping in the MQW structure. The initial EELS data processing was similar to that in the work of Bobynko *et al.*,[61] consisting of energy alignment, trimming of extraneous energy ranges from the datasets where there are no useful data (dominated by readout noise), principal component analysis (PCA), background subtraction, deconvolution to remove plural scattering using the Fourier ratio method (Egerton and Whelan[62]) and mapping using signal integration in a fixed energy window above the edge threshold. For this work, an integration window of 100 eV was used for both the Si-K and Ge-$L_{2,3}$ edges.

Elemental analysis by EELS identifies and quantifies atomic species within the sample using the position and intensity of inner shell energy edges. The atomic concentration, N, can be determined using the following equation:[58]

$$I(\Delta, \beta) = I_0(\Delta, \beta) N \sigma(\Delta, \beta), \tag{1}$$

where I is the intensity of the core loss edge integrated over an energy region Δ starting at the onset of the edge, I_o is the zero loss intensity, N is the areal density of atoms in the area sampled by the beam, $N = nt$ (n is the number of atoms per unit volume and t is thickness of the sample), and σ is the partial ionisation cross section for the acceptance angle β and energy region Δ (for the given beam energy). This is illustrated in Fig. 1 using EELS data from the Ge standard sample.

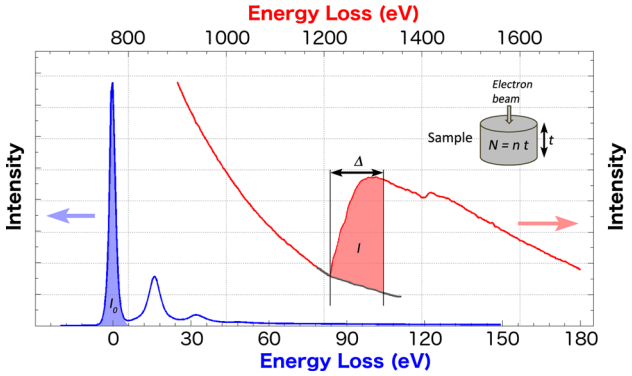

FIG. 1. The low loss (blue) and core loss (red) parts of the EEL spectrum for Ge—the plasmon peak is clearly seen at about 16–17 eV in the low loss, and the $L_{2,3}$ edge for Ge is seen in the red core loss spectrum at around 1200 eV; there is also a small bump at ~1400 eV corresponding to the L_1 edge. The method of signal integration for elemental quantification given by Eq. (1) is shown in the inset. An energy window Δ is used to select signal for the evaluation. The inset shows an electron beam passing through the sample of thickness t, where N represents the areal density of atoms in the area sampled by the electron beam.

The partial ionisation cross section σ is a measure of the probability of inelastic scattering for a specific element. In order to make a quantitative analysis, intensities of the energy edges must be extracted after background subtraction, and the ionisation cross sections must be known if the intensities are to be translated to atomic concentrations. The process can be performed for each pixel of an EELS spectrum image and hence any compositional variations with position can be mapped quantitatively.

The partial ionisation cross section σ can be determined either theoretically or experimentally. Most common theoretical calculations use either hydrogenic or Hartee-Slater models.[63–66] Experimentally, the cross section can be determined from a standard of known composition. This produces accurate results provided the structure and bonding of the standard are similar to the real material and the spectra are acquired under the same conditions. Moreover, the thickness of the region of the standard analysed must be known accurately, together with the number density of the atoms of interest in the standard. There is another approach possible using standards, other than obtaining cross sections, based on k-factor evaluation. For the case of Si-Ge, this would work as follows:

$$\frac{n_{Ge}}{n_{Si}} = \frac{I_{Ge}\sigma_{Si}}{I_{Si}\sigma_{Ge}} = k\frac{I_{Ge}}{I_{Si}}, \tag{2}$$

where $k = \frac{\sigma_{Si}}{\sigma_{Ge}}$. Spectra from the standard, however, and the sample still have to be acquired under the same conditions. Such a method was used effectively by Schade *et al.*[67] for quantification of SiGe islands on Si.

In this work, EELS spectrum images across several repeats in QW structure are quantified by two methods. First, a self-consistent approach has been used which is based simply on using the data from the real Si-Ge MQW specimen to calculate an experimental k-factor on the assumption that it behaves as a simple substitutional alloy. The second approach is a more conventional approach using experimentally determined EELS cross sections using standards from samples of pure Ge and pure Si. The details about these methods are described below.

1. Self-consistent standardless approach for a binary alloy

Due to the difficulties in evaluating cross sections accurately, we developed a self-consistent approach in order to find compositions in the 2-element MQW system. We have assumed that the specimen has a locally constant thickness (i.e., flat surfaces) and that $P_{\mathrm{Ge}} + P_{\mathrm{Si}} = 100\%$ throughout (where P_{X} denotes the atomic percentage of element X), which implies $N_{\mathrm{Ge}} + N_{\mathrm{Si}} = nt$ (assuming a similar atomic number density in all areas). Using Eq. (1) for the two elements in the MQW and then summing them together, the equation results in

$$\frac{I_{Si}}{\sigma_{Si}} + \frac{I_{Ge}}{\sigma_{Ge}} = I_0 nt, \tag{3}$$

where n in this case is the total number of atoms per unit volume, i.e., $n_{\mathrm{Ge}} + n_{\mathrm{Si}}$. Applying Eq. (3) to two points on the scan profile with rather different Si and Ge contents and then equating the two equations leads to the following form:

$$\left(\frac{I_{Si,1}}{\sigma_{Si}} + \frac{I_{Ge,1}}{\sigma_{Ge}}\right)\frac{1}{n_1} = \left(\frac{I_{Si,2}}{\sigma_{Si}} + \frac{I_{Ge,2}}{\sigma_{Ge}}\right)\frac{1}{n_2}. \tag{4}$$

Here, $I_{Si,1}$ and $I_{\mathrm{Si},2}$ are Si edge intensities chosen from two points on the scan profile (near spatially but with rather different compositions), and the same was done for the Ge signal from the same two points. n_1 and n_2 are the values of n at the two points. Rearrangement of Eq. (4) gives

$$\frac{n_1 I_{Ge,2} - n_2 I_{Ge,1}}{n_2 I_{Si,1} - n_1 I_{Si,2}} = \frac{\sigma_{Ge}}{\sigma_{Si}} = k. \tag{5}$$

In the first iteration, it is assumed that n, the number density of atoms, is similar in Ge rich and Si rich regions (probably true to within 2%); this makes $n_1 = n_2$ and thus n cancels in Eq. (5). Using this cross section ratio, k, and ratio of Ge signal to Si signal intensities, i.e., $R = \frac{I_{Ge}}{I_{Si}}$, the Ge and Si percentages, P, at any fixed point can be determined from the following equations:

$$P_{Ge} = \frac{R}{R+k}\%; \quad P_{Si} = \frac{k}{R+k}\%. \tag{6}$$

Using this, the compositions at positions 1 and 2 can then be calculated, the lattice parameters can be obtained for SiGe alloy, with small deviations from Vegard's law, as parametrised by Paul,[68] and then the densities n_1 and n_2 can be explicitly calculated and then Eq. (5) can be recalculated to update the value of k and then Eq. (6) recalculated. As shown below, the iteration converges remarkably rapidly for this case (and presumably any case where the lattice parameter is not a strong function of composition).

2. Cross section determination using standards

For cross sections to be acquired precisely from standards, two issues require extra attention:

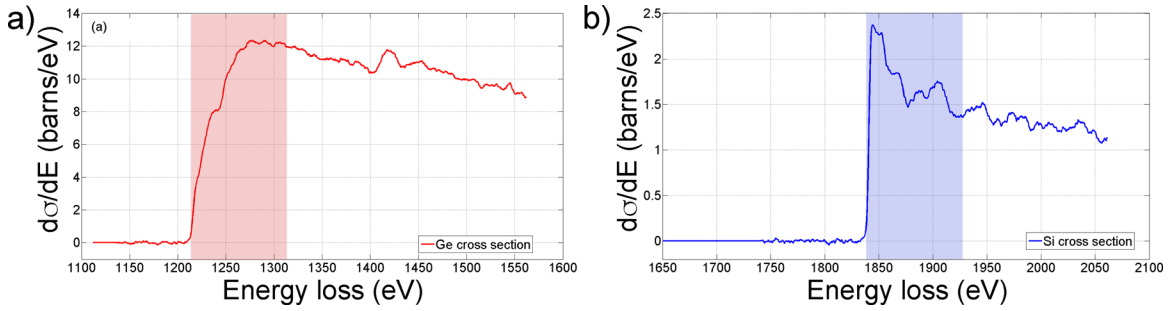

FIG. 2. Differential cross sections determined using least squares fitting of thousands of spectra for (a) the Ge-$L_{2,3}$ edge in pure Ge and (b) the Si-K edge in pure Si. The integration windows used to determine the cross sections were 100 eV in each case.

(a) A thin sample can have a surface layer of significantly different composition to that found in the bulk, which could skew the results for any cross section taken from a standard just calculated from a single spectrum from a single area (no matter how good the data quality). This is taken into account by acquiring data over a range of specimen thickness and then using a least squares fitting technique to extract the bulk behaviour. This is similar to the procedure used previously by Mendis *et al.*[69] and described in detail in the work of Craven *et al.*[70]

(b) The absolute thickness of the sample must be determined accurately. The low loss EELS spectrum provides a map of t/λ for each pixel, which can be used to evaluate the local thickness if λ is known accurately. In this work, the λ values for the Ge and Si standards are obtained from parameterisation of experimental data by Iakoubovskii *et al.*[71] Even if the absolute values of λ calculated by this method are slightly overestimated,[70] the relative values should be correct for two elements with data recorded under identical conditions.

Wedge-shaped specimens from pure Ge and pure Si were used so that data can be taken over a range of thicknesses in order to remove surface layer effects. The value of the cross section at each value of the energy loss was found from a least squares fit using a script written in Digital Micrograph, and recently a similar procedure for vanadium and titanium carbonitrides has been published.[70] This script generates plots of the differential cross section and the corresponding errors from the least squares fit as a function of energy. The fitting was employed for EELS data sets obtained from samples of pure Ge and Si. The extracted differential cross sections were then integrated over an energy window $\Delta = 100$ eV, as indicated in Fig. 2, to produce cross sections suitable for quantifying the experimental data from the MQWs. It should be noted that least square fitting had produced errors in the range of 0.1%–0.35% for each energy channel above the edge threshold for the Ge-L signal. The absolute errors are slightly worse for Si-K, but the percentage errors are a little worse (about 2%), which is unsurprising as it is a weaker edge (K-edge, rather than $L_{2,3}$ so fewer electrons in the transition, and at higher energy) and because background subtraction is a little noisier at the higher energy. The cross sections, σ_{Ge} and σ_{Si}, were obtained from three data sets for each of the standard sample and have been tabulated in Table I. Slight discrepancies were noted between datasets, but these are relatively minor and still allow absolute quantification with errors of just 3%, based on the random error on the Si-K cross section (the dominant error). An average value of each cross section was then used for quantification of MQWs. Atomic concentration of the two elements in MQW system was calculated using the equation given by

$$N_{Si} = \frac{I_{Si}}{I_0 \sigma_{Si}}; \quad N_{Ge} = \frac{I_{Ge}}{I_0 \sigma_{Ge}}. \tag{7}$$

Here, I_{Si} and I_{Ge} were signals obtained from MQW EELS spectra using the same integration window. Again considering that $P_{\mathrm{Ge}} + P_{\mathrm{Si}} = 100\%$ throughout, and using the ratio $r = N_{Ge}/N_{Si}$, the relative percentages, P_{Ge} and P_{Si}, can be determined from the following equations:

$$P_{Ge} = \frac{100\,r}{1+r}\ \%; \quad P_{Si} = \frac{100}{1+r}\ \%. \tag{8}$$

The obtained results have been plotted and compared with those obtained from the self-consistent method in Sec. IV.

IV. RESULTS AND DISCUSSION

A. HAADF-STEM images and thickness profile of QWs

Figure 3(a) shows a typical low magnification HAADF image depicting a highly periodic heterostructure. Since the intensity in HAADF is strongly related to Z, the atomic number, the image clearly demonstrates the difference in the chemistry of the layers. The brighter contrast must be correlated with the Ge QWs, which is confirmed by the EELS results shown later. Superimposed on Fig. 3(a) is a line profile (shown in red) taken over the indicated region as a function of position. This HAADF intensity profile shows some smaller variations over its length but consistently shows that the intensity does not change abruptly at the interface

TABLE I. The cross sections, in barns, for 100 eV windows after the edge onset obtained using least square fitting in Digital Micrograph from three data sets of standard wedge shaped samples of pure Ge and pure Si. The average cross sections given have been used for quantification of the MQW structure.

EELS edge	σ (barns) dataset 1	σ (barns) dataset 2	σ (barns) dataset 3	σ (barns) average
Ge-$L_{2,3}$	976	972	970	973 ± 3
Si-K	171	165	161	166 ± 5

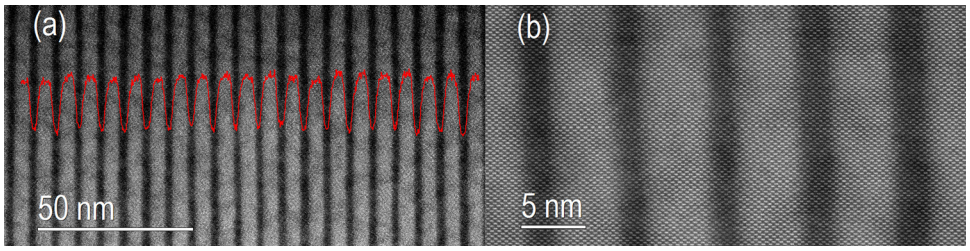

FIG. 3. (a) A HAADF-STEM image of the Ge-GeSi QW superlattice (SL) structure; it clearly distinguishes between the Ge QW and the barrier layer. The red curve is the HAADF intensity profile which shows consistent variations over the given length scale. Each point on this profile is generated from the average of 100 image pixels vertically. (b) A high resolution HAADF-STEM image showing a Ge-rich QW; it is apparent that the interface is diffuse and layers are not uniformly thick across the image.

suggesting some slight intermixing over the length scale. Additionally, the intensity profile may be slightly asymmetric with there being a sharper onset at each interface and a possible slight tailing into the next layer, as has been observed previously.[50,51,72,73] However, this effect is very small and would have a minimal effect on interface width measurement and profile modelling (as is performed below for the EELS and X-ray data).

An atomic resolution HAADF STEM image is shown in Fig. 3(b) recorded along the ⟨110⟩ direction: atomic columns with resolved dumbbells can be clearly observed. It is also quite evident that the Ge QW has fully coherent interfaces with the neighbouring SiGe barrier layers with no obvious discontinuities, dislocations, or bending of atomic planes in the areas observed, suggesting a very low defect density. It is, however, clear as in Fig. 3(a) that the interfaces are not atomically sharp and may also be slightly wavy or stepped. Although a previous study showed that SiGe layers with >28% Ge grown on Si with a thickness greater than 3 monolayers start to roughen,[73] we find that the layers are much less rough, suggesting that the parameters chosen for the growth and the use of the $Si_{0.2}Ge_{0.8}$ buffer layer, which should give a balanced strain, suppress Stranski-Krastanow nucleation of 3D islands, resulting in excellent control of layer flatness over 500 repeats.

On the intermixing at the interfaces, it is well known that in deposition of SiGe layers or pure Ge layers, some Si intermixing can occur during growth.[50,51,74] In STEM studies, however, this appearance of a non-sharp interface can also be attributed to the spreading and dechanneling of the electron beam in the specimen, which can strongly influence the background intensity in HAADF-STEM thereby making atomically sharp interfaces look diffuse.[31,75] Therefore, we have investigated whether there is a real intermixing at the Ge/SiGe interfaces of our MQW system or whether this is simply an effect of beam spreading. This has been done by comparing the measured results with appropriate simulations of beam propagation inside the specimen. Such beam broadening effects have previously been explored, for example, for an InAs/GaAs superlattices.[75]

The actual thickness of the QWs is of great importance since it affects both the electron and heavy hole (HH) energy levels and any change in this thickness affects the overall transition energy (since it affects different energy levels to different degrees), as well as the sensitivity to electric field.[76] Figure 4 represents the thickness profile of both the Ge QW and the SiGe barrier layers plotted against the number of layers; it was obtained by using a line profile generated from the image shown in Fig. 3(a) and defining the interface position as the halfway point in intensity between the maximum for the Ge layer and the minimum for the SiGe layer separated by the interface. Error bars were calculated from an estimated ±1 pixel uncertainty in locating the exact interface centre position. There is clearly some variation in thickness of both the QWs and barrier layers in the stack. Nevertheless, the variation is within the error bars of the measurement, and the Ge QWs show a reasonable uniformity with a thickness of 4.6 ± 0.5 nm, and the barrier layers show a small thickness distribution of 2.6 ± 0.5 nm.

B. Quantitative elemental mapping using DualEELS

In order to acquire information regarding the Ge content, its distribution, and any mixing in MQWs, EELS mapping was performed on the structure where the results are shown in Fig. 5(a). Red corresponds to Ge and is most visible for the QWs, while blue corresponds to Si and is most visible for the barrier layers. The map confirms that the QWs are Ge-rich and the barriers are more Si-rich but there are always a pixel or two of intermediate colours suggesting slight intermixing at the interfaces, which would be consistent with the HAADF contrast shown in Fig. 3.

Figure 5(b) displays the compositional profile of Ge and Si plotted against distance (along representative MQWs), obtained using the self-consistent method (Sec. III B 1). The results obtained from the final iteration (solid line) are plotted together with those obtained from the first iteration

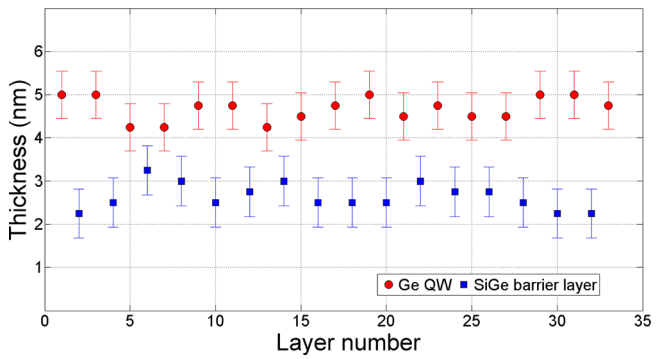

FIG. 4. The thickness profile of the superlattice structure obtained from image analysis. The Ge QWs have an average thickness of 4.6 ± 0.5 nm and the barrier layers are 2.6 ± 0.5 nm thick.

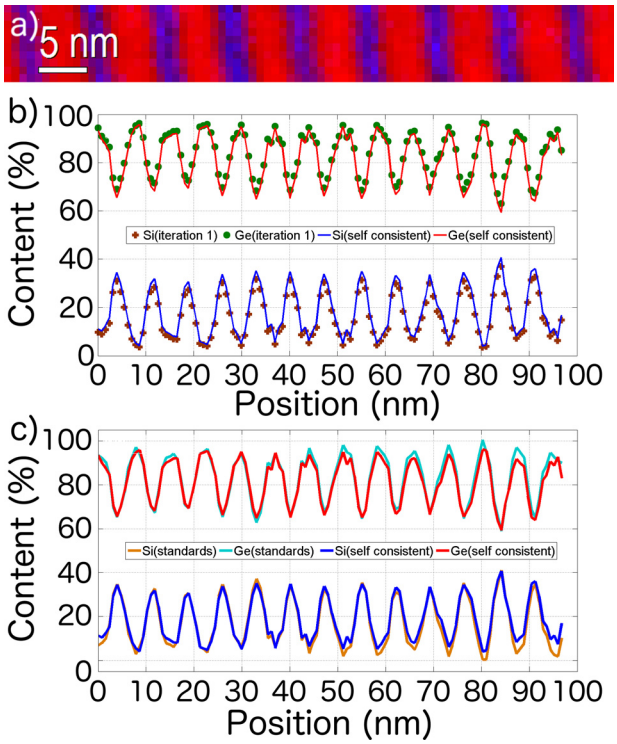

FIG. 5. (a) An elemental map obtained from EELS edge intensities for Ge-$L_{2,3}$ and Si-K from the MQW structure. Red areas are the Ge-rich QWs and blue areas are the Si-rich barrier layers. A slight intermixing at the interface is quite visible. Some drift is also noted in acquisition causing the interfaces to appear not quite vertical. (b) The percentage content along representative MQWs as calculated using the self-consistent method for a one pixel wide profile perpendicular to the interfaces; results obtained from the first iteration (dotted lines) are only slightly different from results after a further iteration (solid lines). (c) A comparison of the compositions in QWs calculated using the self-consistent method (red and blue solid lines) and the experimental cross section method (cyan and gold solid lines).

(dotted line). The difference between the two is very small. In Fig. 5(c), the percentage content calculated using experimental cross sections is compared with the results from the final iteration of the self-consistent method. It is clear that the same trends are seen in both quantification results. There are two reasons why the cross section method might be more reliable. First, the k-factor used in the self-consistent method is just determined from two data points and may be rather susceptible to noise in the data, and this method could clearly be improved by using more data points in estimating the k-factor. Second, it assumes that the surface is flat which could be wrong in a strained layer structure,[77] where the compressively strained Ge layers may bulge outwards slightly normal to the specimen surfaces and the tensile strained SiGe layers may bow inwards slightly. Nevertheless, it clearly shows that such a method could be very useful for a quick and approximate quantification of binary alloy systems, especially where cross sections are not well known and standards of guaranteed composition are difficult to procure. It is clear, however, that using experimentally determined cross sections is preferable if suitable standards can be acquired and prepared in form of wedge-shaped samples. The interaction cross sections should not be affected by surface layers on the standards using the method described above and should be minimally affected by noise in the raw data through calculating them from thousands of individual spectra in one or more spectrum images.

An additional advantage of using the cross section method is that the effective thickness of each element can be determined from the results by calculating N, the areal density of each atomic species using Eq. (1), and then converting this to an effective thickness by dividing by n, the atomic number density. This atomic number density is easily determined from the crystal lattice parameter, a. This was determined using the relationship from Paul[68]

$$a = 0.002733x^2 + 0.01992x + 0.5431, \tag{9}$$

where a is the lattice parameter in nm. n was determined from the standard formula $n = \frac{8}{a^3}$. This resulted in a very constant Si-Ge thickness across the whole area under analysis of about 23 nm, as is shown in more details in the supplementary material (especially in Fig. S3). There was a little extra carbon on the surface in part of this area meaning the total specimen thickness was a little larger.

The plots in Fig. 5 show clearly that QWs are very Ge-rich with a Ge content of around 95%; however, they never reach the level of pure Ge. Also, the Si-content in the barrier layers peaks at about 35%. The intention was that the QWs were 100% Ge and that the barrier layers should be 50% Si. This quantification was undertaken for the top few layers, mid layers, and bottom layers in the stack; results for the top layers are shown here in Fig. 5 and for the rest are given in the supplementary material in Figs. S1 and S2, respectively. All these results are consistent and demonstrate the same compositions for QWs and buffer layers. It is important to mention that results for bottom layers shown in Fig. S2 (supplementary material) also include some buffer layer, which has a Ge content of 80% and Si 20%, as expected from the growth.

It is clear that the Ge composition profiles of Fig. 5 and the HAADF intensity profiles of Fig. 3 are very similar in form and both show somewhat diffuse interfaces with an apparent width of about 4 nm. A quantitative evaluation of the interdiffusion at the barrier/QW interface was performed by fitting the compositional profile in Fig. 5 with a superposition of error functions[78]

$$x = x_b + \frac{1}{2}(x_b - x_w)\left(erf\left(\frac{\frac{h}{2}+x}{\sqrt{2}\sigma}\right) + erf\left(\frac{\frac{h}{2}-x}{\sqrt{2}\sigma}\right)\right), \tag{10}$$

where x_b and x_w are the barrier and QW Ge content, respectively, h is the width of an ideally box-like QW, and σ is the standard deviation which is related to the level of interdiffusion (see supplementary material for the modelling). The value of x_w from the modelling is $95\% \pm 1.7\%$, while the estimation of x_b is affected by a large uncertainty due to the limited thickness of barrier itself (3% errors in the Si-K cross section as noted on page 11 would have no significant effect on this as 3% of 5% is just 0.15%). Reasonable fits can be obtained with x_b in the range of 40%–60%. The QW and barrier thickness obtained from the fitting are 4.7 ± 0.5 nm and 2.6 ± 0.5 nm, respectively. Over a distance $l = 3.3\sigma$, the composition varies from ≈90% of x_b to ≈90% of x_w.

Consequently, l can be taken as a quantitative measure of interface width. The fitting procedure (see supplementary material Fig. S3) gives $\sigma \approx 1$ nm assuming both interfaces around each Ge quantum well are equal and opposite in profile, indicating an interface width $l = 3.3$ nm.

The similarity between the composition profiles and the HAADF profiles is expected since the HAADF contrast will be primarily due to composition at the inner detector angle of 107 mrad. To estimate this width in more detail, the profiles were fitted with an error function as described in the supplementary material and plotted in Fig. S3—this gave a standard deviation for the interface half-width of 0.78 nm. The question that needs asking at this point, however, is how much of this apparent diffuseness is simply a result of beam spreading in the sample and how much is the real sample composition profile? In order to keep the effect of beam spreading as small as possible from the beginning, we chose as thin a sample area as possible for the data acquisition, whilst trying to avoid areas which have suffered from Ga beam damage during the preparation. Measurement of the sample thickness in the areas analysed using EELS was about 23 nm (supplementary material Fig. S3). To investigate the impact of beam broadening on quantification, calculations of electron channelling were made using the Dr. Probe simulation package.[79,80] Table II summarises the predicted beam broadening values calculated at various TEM foil thicknesses. It clearly shows that even for 20 nm, 90% of the probe current is contained in a ring of 0.72 nm radius or 1.4 nm diameter. Extrapolating to 23 nm, this would be 1.6 nm. In comparison to the interface full width (10%–90% of relative composition) measured above of 2.6 nm, it is clear that only about half the apparent width comes from beam broadening. On the assumption that real interdiffusion and beam broadening are totally independent effects, then it is likely that these add in quadrature to create the final observed profile. If that were the case, the real compositional profile would be of the order of $\sqrt{3.3^2 - 1.6^2} = 2.9$ nm. To express this in a standard deviation of the half width, this would be 0.87 nm. It may be noted that some atomic scale roughness is seen at every interface in HRSTEM images such as Fig. 3(b). Nevertheless, this also does not fully explain the measured interface width. Consequently, much of the compositional profile with a standard deviation of 0.78 nm shown in Figs. 3 and 5 represents real interdiffusion between Ge-rich QWs and the Si-rich interlayers.

TABLE II. The calculated beam spreading in the thickness of the sample areas analysed using EELS. $R_{50\%}$ refers to the radius enclosing 50% of the beam current, and $R_{90\%}$ refers to the radius enclosing 90% of the beam current.

Thickness (nm)	$R_{50\%}$ (nm)	$R_{90\%}$ (nm)
0	0.06	0.14
5	0.09	0.22
10	0.17	0.39
15	0.24	0.55
20	0.36	0.72

The fact that the interfaces are not atomically sharp should not be a surprise as several previous studies have reported non-sharp interdiffused interfaces in the Si-Ge systems including in those grown by chemical vapour deposition,[73,81] molecular beam epitaxy,[34] and solvent vapour growth of nanowires.[82] The latter method gave the smallest previously reported interface thickness of about 1 nm (about 2 unit cells) although this was not quantified by fitting and was apparently only from a single point measurement. It is clear, however, that despite differences in growth techniques, Si and Ge are observed to interdiffuse across epitaxial interfaces in all studies performed with sufficient spatial resolution. There are probably two main reasons for this. Firstly and obviously, Si and Ge are isostructural and display complete solid solubility. Secondly, the strain gradient at the interface will be significantly reduced by some interdiffusion spreading out the significant lattice parameter change over a few crystal planes.

In the case of the sample under investigation, a more technical issue might contribute to the smearing out of interfaces. Due to the large number of periods required to perform the optical characterization of intersubband transitions,[25] a relatively high deposition rate of 1 nm/s was used during QW growth. This leads to a switching-time for the supply of precursor gases that might be shorter than the pump-out time and, as a consequence, may have led to the formation of a diffused interface.

Nevertheless, it is clear in the present study that even with this interdiffusion, clearly defined 95% Ge, 5% Si QWs are generated with highly uniform thickness, separated by spacer layers which are approximately 65% Ge, 35% Si at the centre. This is not quite the idealised structure of perfectly defined pure-Ge QWs separated by atomically sharp 50% Ge, 50% Si spacers[25] and some of the Si from the spacers has clearly diffused into the QWs to reduce strain with some Ge diffusing in the reverse direction into the spacers.

C. X-ray diffraction analysis and comparison to STEM data

X-ray diffraction is used as a well-established counterpart to the presented STEM-HAADF and EELS methods. Figure 6 shows a symmetric radial scan along the crystal truncation rod through the (004) Bragg diffraction. The information encoded in these data includes the lattice parameters of the different parts of the multilayer thin film and the chemical composition profile in the MQW. Since the variation of the lattice parameters with the chemical composition and the elastic parameters of SiGe are well known,[83,84] the chemical composition can be exactly determined from the measured lattice parameters. For this purpose, we use a multibeam dynamical theory description[85,86] as implemented in *xrayutilities*[87] to model the experimental data. In order to obtain the match between the simulation and experiment as shown in Fig. 6, we had to include small fluctuations of the period of the MQW and also model the interdiffusion at the interfaces in the MQW. The fluctuations of the period arise from inhomogeneities of growth within the 500 period thick MQW stack and the several mm^2 large spot probed by XRD.

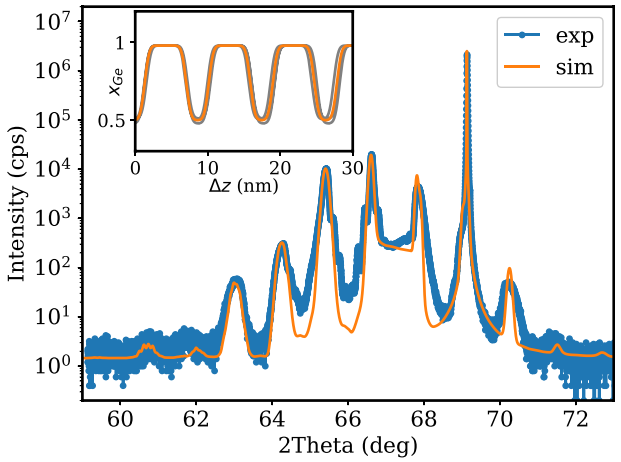

FIG. 6. X-ray diffraction data and simulation near the (004) Bragg peak. Shown are the Si substrate peak along with two peaks of the buffers, which overlap with the periodic diffraction signal of the superlattice (SL) formed by the MQW structure. Using a Ge-profile as shown in the inset with a period thickness of 8.7 ± 0.2 nm and interdiffusion modelled by error functions the experimental data could be reproduced using a dynamical diffraction simulation.

These fluctuations cause broadening of higher order superlattice satellites as observed in Fig. 6. For the particular measurement in Fig. 6, performed on a spot close to the one from which the TEM lamellae were prepared, we find a period thickness of the MQW of 8.7 ± 0.2 nm with an average composition of ~81% which is an excellent match to the composition of the buffer layer (Mark "Buf 2" in Fig. 6) just below the superlattice (SL). Coincidentally, the initial buffer with constant composition around 40% overlaps with one of the SL peaks. From the intensity variation of the SL peaks, one can find the chemical composition profile within the period of the MQW. The inset of Fig. 6 shows the best matching composition profile with 5.4 ± 0.2 nm wells with around 98% Ge and 3.3 ± 0.2 nm barriers. This compares with the values of 4.6 ± 0.5 nm wells and 2.6 ± 0.5 nm barriers from HAADF and 4.7 ± 0.5 nm wells and 2.6 ± 0.5 nm barriers from the modelling of the EELS. The QW/barrier composition and thickness attained by XRD are in reasonably good agreement with those attained by STEM especially if we consider that XRD probes the whole SL stack over an area of several mm^2 while STEM locally investigates a 10–20 nm thick lamella over just ~10–15 periods of the SL. It was also known that there were some small variations in layer thickness across the wafer, and whilst an effort was made to sample comparable areas with XRD and STEM, there may be slight discrepancies in the absolute layer thicknesses for this reason.

An error function like transition region between the barrier and well compositions was needed to obtain the match between simulation and experimental data. The width parameter, σ, of the error function was obtained as 0.7 nm. This compares to 0.87 nm determined from the modelling of the EELS profiles after accounting for beam spreading. It may be that there was more beam spreading in the EELS measurement due to carbon contamination on the surface (as noted in the supplementary material). Nevertheless this demonstrates a pretty good agreement between the X-ray analysis of a larger area of the QW structure and the detailed compositional analysis by EELS of a small area of this structure, and gives us great confidence in our measurements of interdiffusion at the interfaces.

V. CONCLUSION

We have demonstrated quantitative sub-nm structural and chemical characterisation of a Ge/SiGe QW system grown by low energy plasma enhanced chemical vapour deposition (LEPECVD) on high resistivity Si (100), using STEM imaging and EELS. This conclusively demonstrates that despite some slight roughness and thickness variations in layers near the top of the stack of 500 repeats, the Ge-rich QWs are remarkably consistent in thickness at 4.6 ± 0.5 nm separated by Si-rich spacers of thickness 2.6 ± 0.6 nm, and are coherently strained with a very low dislocation density (none were observed). Two methods for quantifying the DualEELS datasets were used and compared. A standardless self-consistent approach was observed to produce results correct to within a few percent in a simple binary alloy system like this. Nevertheless, the most reliable results were found by the use of experimentally determined cross sections for the Si-K and Ge-$L_{2,3}$ edges derived from separate datasets recorded from pure Si and pure Ge specimens. These showed that the QWs are about 95% Ge and 5% Si, whereas the spacers peak at 65% Ge and 35% Si. Both HAADF contrast and EELS elemental profiles show a diffuse interface, and the EELS compositional profile gives an interface standard deviation of the half width about 0.78 nm. This is shown to be mostly a real diffusion profile with very little effect from beam spreading in the specimen. The EELS measurements are in excellent agreement with X-ray diffraction, which gives an average interface standard deviation across the whole area of about 0.7 nm. This shows that if pure or nearly pure Ge QWs are required that are thinner than this, the growth procedure will have to be modified to reduce this interdiffusion profile.

SUPPLEMENTARY MATERIAL

See supplementary material for composition across the mid and bottom layers in the MQW structure investigated, together with fitting of the compositional profile to determine the apparent interface width (including both real contributions from interdiffusion and contributions from electron beam spreading in the sample).

ACKNOWLEDGMENTS

A.B. is thankful to the Schlumberger Foundation Faculty for the Future programme for the provision of a research fellowship. We are grateful to SUPA and the University of Glasgow for the provision of the JEOL ARM200F microscope used in this work. The material design and growth leading to the results has received funding from the European Union's 7th Framework Programme through the GEMINI Project (Project No. 613055). J.B. thankfully acknowledges support from the Deutsche Forschungsgemeinschaft (DFG) by the core facilities Grant No. MA 1280/40-1. D.J.P. is thankful

to the EPSRC for Funding (No. EP/N003225/1). D.K. acknowledges the support from the ERDF (Project No. CZ.02.1.01/0.0/0.0/15_003/0000485) and the Grant Agency of the Czech Republic Grant (No. 14-37427G). We are also grateful to Professor A. J. Craven for helpful discussions and the provision of the script used in this work for the calculation of the EELS cross sections.

[1]D. A. B. Miller and H. M. Ozaktas, J. Parallel Distrib. Comput. **41**(1), 42–52 (1997).
[2]D. A. B. Miller, Proc. IEEE **88**(6), 728–749 (2000).
[3]J. Michel, J. F. Liu, and L. C. Kimerling, Nat. Photonics **4**(8), 527–534 (2010).
[4]H. T. Lin, O. Ogbuu, J. F. Liu, L. Zhang, J. Michel, and J. J. Hu, J. Lightwave Technol. **31**(24), 4029–4036 (2013).
[5]E. Timurdogan, C. M. Sorace-Agaskar, J. Sun, E. S. Hosseini, A. Biberman, and M. R. Watts, Nat. Commun. **5**, 4008 (2014).
[6]M. W. Geis, S. J. Spector, M. E. Grein, J. U. Yoon, D. M. Lennon, and T. M. Lyszczarz, Opt. Express **17**(7), 5193–5204 (2009).
[7]K. Y. Cheng, R. Anthony, U. R. Kortshagen, and R. J. Holmes, Nano Lett. **11**(5), 1952–1956 (2011).
[8]Y. H. Kuo, Y. K. Lee, Y. S. Ge, S. Ren, J. E. Roth, T. I. Kamins, D. A. B. Miller, and J. S. Harris, Nature **437**(7063), 1334–1336 (2005).
[9]D. Ahn, C. Y. Hong, J. F. Liu, W. Giziewicz, M. Beals, L. C. Kimerling, J. Michel, J. Chen, and F. X. Kartner, Opt. Express **15**(7), 3916–3921 (2007).
[10]J. Liu, M. Beals, A. Pomerene, S. Bernardis, R. Sun, J. Cheng, L. C. Kimerling, and J. Michel, Nat. Photonics **2**(7), 433–437 (2008).
[11]J. F. Liu, X. C. Sun, R. Camacho-Aguilera, L. C. Kimerling, and J. Michel, Opt. Lett. **35**(5), 679–681 (2010).
[12]D. C. S. Dumas, K. Gallacher, S. Rhead, M. Myronov, D. R. Leadley, and D. J. Paul, Opt. Express **22**(16), 19284 (2014).
[13]Y. Cai, Z. H. Han, X. X. Wang, R. E. Camacho-Aguilera, L. C. Kimerling, J. Michel, and J. F. Liu, IEEE J. Sel. Top. Quantum Electron. **19**(4), 9 (2013).
[14]M. Bollani, D. Chrastina, V. Montuori, D. Terziotti, E. Bonera, G. M. Vanacore, A. Tagliaferri, R. Sordan, C. Spinella, and G. Nicotra, Nanotechnology **23**(4), 045302 (2012).
[15]D. A. B. Miller, Proc. IEEE **97**(7), 1166–1185 (2009).
[16]G. T. Reed, G. Mashanovich, F. Y. Gardes, and D. J. Thomson, Nat. Photonics **4**(8), 518–526 (2010).
[17]E. H. Edwards, L. Lever, E. T. Fei, T. I. Kamins, Z. Ikonic, J. S. Harris, R. W. Kelsall, and D. A. B. Miller, Opt. Express **21**(1), 867–876 (2013).
[18]J. Frigerio, P. Chaisakul, D. Marris-Morini, S. Cecchi, M. S. Roufied, G. Isella, and L. Vivien, Appl. Phys. Lett. **102**(6), 061102 (2013).
[19]J. Frigerio, V. Vakarin, P. Chaisakul, M. Ferretto, D. Chrastina, X. Le Roux, L. Vivien, G. Isella, and D. Marris-Morini, Sci. Rep.-UK **5**, 8 (2015).
[20]P. Chaisakul, D. Marris-Morini, J. Frigerio, D. Chrastina, M. S. Rouifed, S. Cecchi, P. Crozat, G. Isella, and L. Vivien, Nat. Photonics **8**(6), 482–488 (2014).
[21]E. Gatti, E. Grilli, M. Guzzi, D. Chrastina, G. Isella, and H. von Kanel, Appl. Phys. Lett. **98**(3), 031106 (2011).
[22]K. Gallacher, P. Velha, D. J. Paul, S. Cecchi, J. Frigerio, D. Chrastina, and G. Isella, Appl. Phys. Lett. **101**(21), 211101 (2012).
[23]O. Fidaner, A. K. Okyay, J. E. Roth, R. K. Schaevitz, Y. H. Kuo, K. C. Saraswat, J. S. Harris, and D. A. B. Miller, IEEE Photonics Technol. Lett. **19**(17–20), 1631–1633 (2007).
[24]E. Onaran, M. C. Onbasli, A. Yesilyurt, H. Y. Yu, A. M. Nayfeh, and A. K. Okyay, Opt. Express **20**(7), 7608–7615 (2012).
[25]K. Gallacher, A. Ballabio, R. W. Millar, J. Frigerio, A. Bashir, I. MacLaren, G. Isella, M. Ortolani, and D. J. Paul, Appl. Phys. Lett. **108**(9), 091114 (2016).
[26]D. J. Paul, J. Appl. Phys. **120**(4), 043103 (2016).
[27]L. K. Nanver, V. Jovanovic, C. Biasotto, J. Moers, D. Gruetzmacher, J. J. Zhang, N. Hrauda, M. Stoffel, F. Pezzoli, O. G. Schmidt, L. Miglio, H. Kosina, A. Marzegalli, G. Vastola, G. Mussler, J. Stangl, G. Bauer, J. van der Cingel, and E. Bonera, Solid-State Electron. **60**(1), 75–83 (2011).
[28]W. Potz and Z. Q. Li, Solid-State Electron. **32**(12), 1353–1357 (1989).
[29]T. Das and S. Bhattacharyya, Microsc. Microanal. **17**(5), 759–765 (2011).
[30]S. Cosentino, A. M. Mio, E. G. Barbagiovanni, R. Raciti, R. Bahariqushchi, M. Miritello, G. Nicotra, A. Aydinli, C. Spinella, A. Terrasi, and S. Mirabella, Nanoscale **7**(26), 11401–11408 (2015).
[31]K. A. Mkhoyan, E. J. Kirkland, J. Silcox, and E. S. Alldredge, J. Appl. Phys. **96**(1), 738–746 (2004).
[32]H. Kauko, T. Grieb, R. Bjorge, M. Schowalter, A. M. Munshi, H. Weman, A. Rosenauer, and A. T. J. van Helvoort, Micron **44**, 254–260 (2013).
[33]M. Tewes, F. F. Krause, K. Mueller, P. Potapov, M. Schowalter, T. Mehrtens, and A. Rosenauer, in *18th Microscopy of Semiconducting Materials Conference*, edited by T. Walther and J. L. Hutchison (IOP, 2013), Vol. 471.
[34]M. Brehm, H. Groiss, G. Bauer, D. Gerthsen, R. Clarke, Y. Paltiel, and Y. Yacoby, Nanotechnology **26**(48), 485702 (2015).
[35]Y. Cho, J. S. Park, J. M. Yang, K. J. Park, Y. C. Park, J. Chang, S. G. Lee, and K. Y. Han, J. Mater. Res. **30**(19), 2893–2899 (2015).
[36]K. Thompson, J. H. Bunton, J. S. Moore, and K. S. Jones, Semicond. Sci. Technol. **22**(1), S127–S131 (2007).
[37]A. Grenier, S. Duguay, J. P. Barnes, R. Serra, G. Haberfehlner, D. Cooper, F. Bertin, S. Barraud, G. Audoit, L. Arnoldi, E. Cadel, A. Chabli, and F. Vurpillot, Ultramicroscopy **136**, 185–192 (2014).
[38]M. Gilbert, W. Vandervorst, S. Koelling, and A. K. Kambham, Ultramicroscopy **111**(6), 530–534 (2011).
[39]D. Blavette, P. Duval, L. Letellier, and M. Guttmann, Acta Mater. **44**(12), 4995–5005 (1996).
[40]M. K. Miller and M. G. Hetherington, Surf. Sci. **246**(1–3), 442–449 (1991).
[41]V. Grillo, E. Carlino, and F. Glas, Phys. Rev. B **77**(5), 054103 (2008).
[42]M. Herrera, Q. M. Ramasse, D. G. Morgan, D. Gonzalez, J. Pizarro, A. Yanez, P. Galindo, R. Garcia, M. H. Du, S. B. Zhang, M. Hopkinson, and N. D. Browning, Phys. Rev. B **80**(12), 125211 (2009).
[43]V. Grillo, Ultramicroscopy **109**(12), 1453–1464 (2009).
[44]C. Jeanguillaume and C. Colliex, Ultramicroscopy **28**(1–4), 252–257 (1989).
[45]J. A. Hunt and D. B. Williams, Ultramicroscopy **38**(1), 47–73 (1991).
[46]J. Scott, P. J. Thomas, M. MacKenzie, S. McFadzean, J. Wilbrink, A. J. Craven, and W. A. P. Nicholson, Ultramicroscopy **108**(12), 1586–1594 (2008).
[47]I. M. Ross, M. Gass, T. Walther, A. Bleloch, A. G. Cullis, L. Lever, Z. Ikonic, M. Califano, R. W. Kelsall, J. Zhang, and D. J. Paul, in *Microscopy of Semiconducting Materials 2007*, edited by A. G. Cullis and P. A. Midgley (Springer-Verlag Berlin, Berlin, 2008), Vol. 120, pp. 269.
[48]P. Longo, D. J. Stowe, R. D. Twesten, and A. Howkins, Microsc. Microanal. **21**(S3), 1259–1260 (2015).
[49]T. Walther, C. J. Humphreys, and D. J. Robbins, Defect Diffus. Forum **143–147**, 1135–1140 (1997).
[50]T. Walther and C. J. Humphreys, J. Cryst. Growth **197**(1–2), 113–128 (1999).
[51]D. J. Norris, A. G. Cullis, T. J. Grasby, and E. H. C. Parker, J. Appl. Phys. **86**(12), 7183–7185 (1999).
[52]R. Pantel, S. Jullian, D. Delille, D. Dutartre, A. Chantre, O. Kermarrec, Y. Campidelli, and L. Kwakman, Micron **34**(3–5), 239–247 (2003).
[53]S. Cecchi, E. Gatti, D. Chrastina, J. Frigerio, E. M. Gubler, D. J. Paul, M. Guzzi, and G. Isella, J. Appl. Phys. **115**(9), 093502 (2014).
[54]M. Schaffer, B. Schaffer, and Q. Ramasse, Ultramicroscopy **114**, 62–71 (2012).
[55]L. Jones and P. D. Nellist, Microsc. Microanal. **19**(4), 1050–1060 (2013).
[56]D. A. Muller, E. J. Kirkland, M. G. Thomas, J. L. Grazul, L. Fitting, and M. Weyland, Ultramicroscopy **106**(11–12), 1033–1040 (2006).
[57]K. Kimoto, T. Asaka, X. Z. Yu, T. Nagai, Y. Matsui, and K. Ishizuka, Ultramicroscopy **110**(7), 778–782 (2010).
[58]I. MacLaren, R. Villaurrutia, B. Schaffer, L. Houben, and A. Pelaiz-Barranco, Adv. Funct. Mater. **22**(2), 261–266 (2012).
[59]L. Jones, H. Yang, T. J. Pennycook, M. S. J. Marshall, S. Van Aert, N. D. Browning, M. R. Castell, and P. D. Nellist, Adv. Struct. Chem. Imaging **1**, 8 (2015).
[60]B. Schaffer, W. Grogger, and G. Kothleitner, Ultramicroscopy **102**(1), 27–36 (2004).
[61]J. Bobynko, I. MacLaren, and A. J. Craven, Ultramicroscopy **149**, 9–20 (2015).
[62]R. F. Egerton and M. J. Whelan, J. Electron Spectrosc. Relat. Phenom. **3**(3), 232–236 (1974).
[63]R. D. Leapman, P. Rez, and D. F. Mayers, J. Chem. Phys. **72**(2), 1232–1243 (1980).
[64]R. F. Egerton, J. Microsc.-Oxford **123**, 333–337 (1981).
[65]R. F. Egerton, Ultramicroscopy **50**(1), 13–28 (1993).
[66]R. F. Egerton, *Electron Energy-Loss Spectroscopy in the Electron Microscope* (Springer, New York, 2011).
[67]M. Schade, F. Heyroth, F. Syrowatka, H. S. Leipner, T. Boeck, and M. Hanke, Appl. Phys. Lett. **90**(26), 263101 (2007).
[68]D. J. Paul, Laser Photonics Rev. **4**(5), 610–632 (2010).

[69]B. G. Mendis, M. MacKenzie, and A. J. Craven, Ultramicroscopy **110**(2), 105–117 (2010).
[70]A. J. Craven, J. Bobynko, B. Sala, and I. MacLaren, Ultramicroscopy **170**, 113–127 (2016).
[71]K. Iakoubovskii, K. Mitsuishi, Y. Nakayama, and K. Furuya, Microsc. Res. Tech. **71**(8), 626–631 (2008).
[72]A. Benedetti, D. J. Norris, C. J. D. Hetherington, A. G. Cullis, D. J. Robbins, and D. J. Wallis, J. Appl. Phys. **93**(7), 3893–3899 (2003).
[73]D. J. Norris, Y. Qiu, A. Dobbie, M. Myronov, and T. Walther, J. Appl. Phys. **115**(1), 012003 (2014).
[74]M. Brehm, M. Grydlik, H. Lichtenberger, T. Fromherz, N. Hrauda, W. Jantsch, F. Schaeffler, and G. Bauer, Appl. Phys. Lett. **93**(12), 121901 (2008).
[75]P. D. Robb, M. Finnie, P. Longo, and A. J. Craven, Ultramicroscopy **114**, 11–19 (2012).
[76]R. K. Schaevitz, J. E. Roth, S. Ren, O. Fidaner, and D. A. B. Miller, IEEE J. Sel. Top. Quantum Electron. **14**(4), 1082–1089 (2008).
[77]J. M. Gibson and M. M. J. Treacy, Ultramicroscopy **14**(4), 345–349 (1984).
[78]J. Crank, *The Mathematics of Diffusion* (Oxford Science Publications, Oxford, UK, 1980).
[79]J. Barthel "Dr. Probe - High-resolution (S)TEM image simulation software," http://www.er-c.org/barthel/drprobe/ (2016).
[80]J. Barthel, *Time-efficient frozen phonon multislice calculations for image simulations in high-resolution STEM*. in *15th European Microscopy Congress* (Manchester, 2012).
[81]T. Walther, C. J. Humphreys, and A. G. Cullis, Appl. Phys. Lett. **71**(6), 809–811 (1997).
[82]H. Geaney, E. Mullane, Q. M. Ramasse, and K. M. Ryan, Nano Lett. **13**(4), 1675–1680 (2013).
[83]J. P. Dismukes, R. J. Paff, and L. Ekstrom, J. Phys. Chem. **68**(10), 3021 (1964).
[84]F. Schaffler, in *Properties of Advanced Semiconductor Materials GaN, AlN, InN, BN, SiC, SiGe*, edited by M. E. Levinshtein, S. L. Rumyantsev, and M. S. Shur (John Wiley & Sons, Inc., New York, 2001), pp. 149–188.
[85]C. G. Darwin, Philos. Mag. **27**(157–62), 315–333 (1914).
[86]S. L. Morelhao, C. I. Fornari, P. H. O. Rappl, and E. Abramof, J. Appl. Crystallogr. **50**, 399–410 (2017).
[87]D. Kriegner, E. Wintersberger, and J. Stangl, J. Appl. Crystallogr. **46**, 1162–1170 (2013).